Research Article Vol. 3, No. 8 / 15 August 2020 / OSA Continuum 2062

Ultra-long light sheets via curved beam intercrossing

ENRIQUE G. NEYRA,[1] ÓSCAR MARTÍNEZ-MATOS,[2] AND PABLO VAVELIUK[1,2,*]

[1] *Centro de Investigaciones Ópticas (CICBA-CONICET-UNLP), Cno. Parque Centenario y 506, P.O. Box 3, 1897 Gonnet, Argentina*
[2] *Departamento de Óptica, Facultad de Ciencias Físicas, Universidad Complutense de Madrid, Av. Complutense s/n, 28040 Madrid, Spain*
[*] *pablov@ciop.unlp.edu.ar*

Abstract: An approach to yield a planar light sheet with thickness below the Abbe's diffraction limit over ultra-long propagation distances is presented. Such features emerge by an induced interference of the fields associated to the caustic branches of a cusp-type curved beam. The optical sheet width and length are dynamically tuned by just varying one parameter of the signal encoded in a spatial light modulator within a standard setup for curved beam generation. This light sheet possesses the following characteristics: a high length-to-width ratio, a width below the Abbe's diffraction limit, reduced sidelobes, and very low spreading along the sheet length. These planar light sheets could be useful in light-sheet microscopy and applications to surface and interface physics. In addition, these sheets can be easily transformed in an optical needle having rectangular symmetry by using a two-dimensional cusp beam instead of an one-dimensional beam.

1. Introduction

An ultra-long optical needle is a beam that exhibits ultra-long light focus much grater than its cross-sectional dimension [1,2]. Usually the beam thickness is compared with a reference dimension given by the Abbe's length, also called the Abbe's diffraction limit [3], $0.5\lambda/\mathrm{NA}$, being λ the wavelength and NA the numerical aperture. Needles that exhibit thickness below the Abbe's length are useful for imaging, optical manipulation and trapping of particles, lithography, medical applications, laser drilling and for carrying information at very small scale over long trajectories [4–11]. The design of optical needles below the Abbe's length is performed in an axial-cylindrical frame and was tackled by a wide number of research groups by several ingenious methods [12–27]. The central matter of these approaches was to achieve the greatest length-to-width ratio for the needle. This ratio acts as a figure of merit to evaluate the needle performance, achieving values from a few units to several orders of magnitude [12,13,15,16,18–22,24–27]. When an optical needle with thickness below the Abbe's length is extended along one transverse axis, it becomes an "optical razor blade" (ORB), i.e. an ultra-long light sheet having a thickness below the Abbe's diffraction limit.

Light Sheets (LSs) are mainly used in light sheet microscopy (LSM) as the excitation source [28]. In this application, LSs are usually generated by focusing Gaussian or top-hat beams using a cylindrical lens or by quickly moving an exotic beam, often a Bessel or an Airy beam, along a transverse axis forming a "virtual" LS [28]. The length and width of the LS are related to the figures of merit of LSM, namely the field of view (FOV) and the axial resolution (AR), respectively. The challenge is then to achieve a versatile and easy-to-implement method to obtain a real LS having ultra-long sub-Abbe's length features with high performance in FOV and AR. This could benefit the LSM in addition to fit the 2D geometry of interfaces extending the spectrum of applications to physics of surfaces and interfaces.

#393073 https://doi.org/10.1364/OSAC.393073
Journal © 2020 Received 14 Apr 2020; revised 1 Jul 2020; accepted 1 Jul 2020; published 31 Jul 2020

OSA CONTINUUM

This work reports on a method to design ORBs with thickness below the Abbe's diffraction limit over ultra-long propagation distances. This proposal is based on a different viewpoint regarding the current methods used to design optical needles and light sheets, as well. Specifically, the approach benefits on a controllable manipulation of the optical fields tied to the branches of a cusp-type caustic curve. The ORB arises due to an induced interference of the branch fields occurring in the closeness of the intercrossing of the caustic branches, giving rise to a linear focus along the propagation coordinate z of thickness in the x-coordinate that extends along the y-coordinate. The analysis is done in the xz-plane since the light sheet is achieved in the yz-plane by trivial extension along y-coordinate. We demonstrate an ORB with a high length-to-width ratio greater than 640 with reduced sidelobes. The thickness narrowing is tuned by laterally displacing the caustic branches which in turn shifts the intercrossing point and modifies the interference pattern. This shift is digitally controlled varying a single parameter of the spectral phase encoded into a Spatial Light Modulator (SLM) within a standard setup for curved beam generation [29].

2. Theoretical foundations

According to the Catastrophe Theory [30], the caustic curve is the envelope of a family of rays along which the wave oscillation has exceptionally large magnitude to abruptly decay to zero beyond it. The caustic can be viewed as the "skeleton" of the beam intensity. A cusp-type caustic is a curve in the xz-plane having two specular branches originating from a common point, the cusp point (CP) as illustrated by dashed lines in Fig. 1. The transverse coordinate is x and the propagation one is z. Both are scaled by characteristic lengths, x_0 and $z_0 = (2\pi/\lambda)x_0^2$, defined by the experimental setup, being λ the wavelength. The cusp caustic is generated from the 1D even spectral phase [31], $\psi(K) = \gamma\,|K|^3$ (top inset in Fig. 1), where $K = x_0\kappa$ is the dimensionless frequency, κ is the spatial frequency and the parameter γ is the dimensionless parameter that defines the rate of variation of the spectral phase. The phase ψ gives rise to a cusp caustic with parabolic branches that is the skeleton of the symmetric Airy beam (SAB) [32], whose intensity map in the xz-plane is also depicted in the top inset of Fig. 1. Each point belonging to the caustic, namely (x_c, z_c), have a one to one correspondence with the generatrix frequency K_c, that cancels the two first derivatives of the full phase term in the diffraction integral [30,31]. The caustic curve can be derived by parametric equations of the ψ-derivatives evaluated at K_c [33,34]. Explicitly,

$$x_c(K_c) = x_0\left[K\,\left(d^2\psi/dK^2\right) - (d\psi/dK)\right]_{K=K_c}, \tag{1a}$$

$$z_c(K_c) = z_0\left(d^2\psi/dK^2\right)_{K=K_c}. \tag{1b}$$

One branch (green dashed line) is generated from $K_c>0$ while the other (red dashed line), from $K_c<0$. The central frequency $K_c = 0$ sets the CP at $(0, 0)$. The caustic points appear further from the CP as the frequency value increases (in absolute value). As it is observed in the top inset of Fig. 1, the interference of the branch fields in the closeness of CP gives rise to the SAB autofocus [32]. The superposition of an even linear phase to ψ yields the new phase: $\psi^\dagger = \psi + \alpha\,|K|$, that generates the ORB (both shown in bottom inset of Fig. 1), where α is the perturbation strength. The phase $\psi^\dagger$ laterally shifts the branches in opposite senses a distance α (in x/x_0-scale), depicted by continuum lines in Fig. 1, breaking the original cusp structure. The intersection point z_{in}, generated by frequency K_{in}, lies on the z-axis. The ORB, which is formed in the yz-plane, arises from the interference of the fields tied to the caustic branches. Its thickness narrows to higher K_{in} according to Fourier optics [35]. The intensity map of the ORB in the xz-plane is displayed in bottom inset of Fig. 1. The caustic intercrossing is also suitable to yield the abruptly autofocusing phenomenon [34]. On the other hand, the constraint $x_c = 0$ yields $K_{in} = \pm\sqrt{\alpha/(3\gamma)}$ and $z_{in} = 6\,z_0\gamma\,|K_{in}| = 2z_0\sqrt{3\alpha\,\gamma}$. Once γ is fixed, K_{in} and z_{in} are determined by α, being able to

OSA CONTINUUM

be externally controlled by means of a SLM. The increment of α modifies the ORB features in two ways: 1) By reducing the ORB thickness since K_{in} increases; 2) By shortening the sheet due to a higher caustic intersection aperture. Since one expects narrower widths and larger lengths, there is a competition between both ORB features that is controlled by the key parameter α.

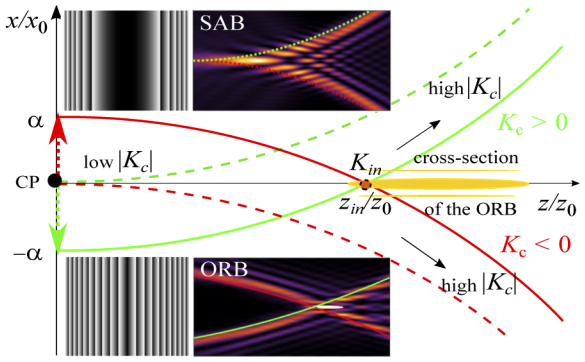

Fig. 1. Representation of the ORB generated from the SAB (shown in the xz-plane). The LS occurs in the yz-plane. The cusp caustic tied to the SAB (dashed line) becomes a caustic with laterally displaced branches (continuum line) when an even linear phase is superposed to the SAB phase. The phase perturbation strength α fixes the branch displacement. The ORB emerges along z-axis, in the closeness of z_{in}/z_0. Top inset: SAB phase mask, scale: 0 (black), 2π (white) and intensity map, scale: maximum intensity (bright), zero intensity (dark). Bottom inset: ORB phase mask and intensity map.

The generation of the ORB can be described from the wave field interference. In the angular spectrum picture [35], the fields u_{K^+} and u_{K^-}, related to the branches $K_c>0$ and $K_c<0$, respectively, can be written in the xz-plane, except for a dimensional constant, as

$$u_{K^+(K^-)}(x,z) = e^{-i(2\pi/\lambda)z} \int_{0\,(-\infty)}^{\infty\,(0)} A(K) e^{i\psi^\dagger(K)}\; e^{-iK^2\frac{z}{2z_0}}\; e^{iK\frac{x}{x_0}}\, dK, \tag{2}$$

where $A(K)$ is the real spectral amplitude on the SLM. The interference between both fields occurs along the z-axis for $z>z_{in}$ giving rise to the needle focus, as the bottom inset of Fig. 1 shows. This is described by the intensity

$$I = |u_{K^+} + u_{K^-}|^2 = I_{K^+} + I_{K^-} + I_{cr}, \tag{3}$$

where $I_{K^+(K^-)} = |u_{K^+(K^-)}|^2$ and the interference term $I_{cr} = 2\mathrm{Re}[u_{K^+}\, u^*_{K^-}]$. Equations (2–3) are used for performing the numerical analysis of the needle focus dynamics in terms of α.

3. Experimental setup

In the experiment, a *top-hat* laser beam of homogeneous intensity of diameter D = 8mm and wavelength λ = 532nm impinges on a reflection SLM (Pluto Holoeye VIS-016-HR version 8-bit gray-level, pixel pitch of 8 μm, 1920 × 1080 pixels, calibrated for a 2π phase shift) in which was addressed a 1D phase mask $\psi^\dagger(K;\gamma,\alpha)$ that generates the SAB for $\alpha = 0$ (top inset in Fig. 1) and the ORB for $\alpha \neq 0$ (bottom inset in Fig. 1). The reflected beam from the SLM was focused by a cylindrical convergent lens (focal length f = 50cm, N-BK7 glass). The beam propagation around the focal region was measured by a CMOS camera (DCC1545M Thorlabs, 8-bit gray-level, pixel pitch of 5.2 μm, 1280 × 1024 pixels). The spectral phase was encoded onto the SLM with a number of wraps, N, given by $N = \psi(K_{lim})/2\pi = \gamma|K_{lim}|^3/2\pi$, that depends

OSA CONTINUUM

on the limit (maximum) value of the dimensionless frequency, K_{lim}, and on the parameter γ. The effective spatial frequency range on the SLM, ($-\kappa_{lim}$, κ_{lim}), can be determined from the band-limited frequency $\kappa_{lim} = \pi D/\lambda f$. For the values of D, f and λ corresponding to the current setup, $\kappa_{lim} = 0.095\mu\text{m}^{-1}$. As the characteristic length scale was fitted to be $x_0 = 39.2\mu$m, we obtain $K_{lim} = \kappa_{lim} x_0 = \pm 3.73$. The number of wraps in $D/2$ was designed to be $N = 5.3$ such that the parameter γ finally gives $\gamma = 5.3 \times 2\pi/K_{lim}^3 = 0.643$. We measure the intensity of the ORB on successive transverse planes, each 0.2mm over 10cm length for each α-value. These measurements were performed for several values of α, ranged in $[0, 16]$ with steps of unit.

4. Results and discussions

The ORB performance as a function of α is centred on the behavior of the full width at half maximum (FWHM) of the intensity profile on-x-axis at the waist plane (z-position of largest intensity), namely Δx_w, and on the FWHM of the intensity along z-axis, namely Δz. The results are presented in Fig. 2(a) and (b). Red dots corresponds to experimental values while the black dot line denotes the numerical ones remarking the good agreement for both features. The Abbe's diffraction limit for the top-hat beam, with dimension equal to the SLM aperture, passing through a cylindrical lens (1D rectangular symmetry) is given by the distance from the peak intensity to the first zero of the sinc-squared pattern that is the intensity of the 1-D top-hat Fourier transform. We obtain the value $d = 0.5\lambda/\text{NA} = 33.25$ μm where NA=$(D/2f) = 0.008$ is the numerical aperture. This transverse thickness in terms of the FWHM was calculated to be $\Delta x_F = 0.886\, d \approx 29.5$ μm (blue dashed line). From subfigure (a), the increment of α decreases Δx_w, becoming shorter than Δx_F at $\alpha = \alpha_{\tilde{F}} \approx 5.8$. One has a width below the Abbe's diffraction limit for $\alpha > \alpha_F$, and it gets narrower as α increases. For the maximum experimental value, $\alpha = 16$, the narrowest width close to 21μm was obtained. This implies a reduction of almost 32% of Δx_F. The increment of α implies higher K_{in} triggering, in turn, a narrowing of the ORB thickness, as it has been shown. On the other hand, from subfigure (b), the increment of α also decreases the length Δz. The decrease rate quickly diminishes up to $\alpha \approx 8$. From this point the reduction becomes very slow. In the α-range $(11, 16)$, Δz is practically constant varying from 15.6 to 12.8 mm, being this later the shorter length obtained. Both light sheet features are used to determine the length-to-width ratio in the xz-plane, $R = \Delta z/\Delta x_w$ that is the figure of merit to evaluate the performance of the ORB. Greater R implies ORBs with better performance. The inset in subfigure (b) shows the behavior of R against α. Notice that from $\alpha > 10$, one has $\Delta x_w < 25$ μm and a practically constant R-value with $R > 640$. It is thus demonstrated a high length-to-width ratio as high as the greatest values reported for circularly symmetric needles [15,16,21,22,26,27]. Theoretical efforts have been made to extend R to much greater values [36], but there is not yet experimental evidence. Our proposal is simple and robust and the scope is broad since it can be applied for any type of rectangular-symmetric caustic beams beyond the cusp-type beam [37]. In addition, the method allows 2D ultra-long needle generation below the Abbe's diffraction limit by just encoding a proper 2D spectral phase into the SLM and by changing the cylindrical lens by a spherical one in the setup.

The next step is to evaluate the nondiffracting properties of the ORB. This analysis is performed for $\alpha = 11$. Figure 3(a) depicts a numerical simulation in the xz-plane beginning from the Fourier plane of the cylindrical lens ($z = 0$). The caustic curves calculated from Eq. (1) are represented by dotted blue lines. The source code for these calculations, written in Mathematica language, is available in Code 1 [38]. The ORB emerges in the closeness of z_{in} due to the interference process of the fields tied to the caustic branches. The different scales for transverse (μm) and propagation (mm) coordinates highlight the ultra-long nature of the LS. To analyze in detail the focus region, subfigs. (b) (numerical simulation) and (c) (experiment) show a zoom of the framed region of (a). The good agreement between theory and experiment is apparent. We determine the ORB thickness and length features obtaining $\Delta x_w \approx 24.3\mu$m at the LS waist and $\Delta z \approx 15.5$ mm, such

OSA CONTINUUM

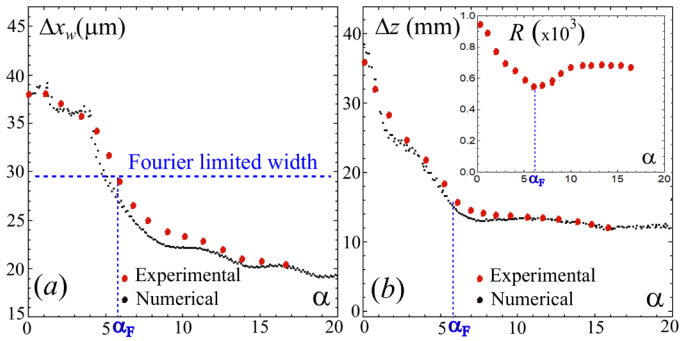

Fig. 2. FWHM of the ORB intensity: (a) along the x-axis at its waist ($z = z_w$) and (b) along the z-axis (at $x = 0$) vs. α. The inset depicts the ORB length-to-width ratio against α.

that R>640, confirming the ultra-long nature of the ORB. Another key magnitude for evaluating the LS performance is the sidelobe-to-central lobe intensity ratio, say r, since sidelobes yield unwanted effects in LS applications. Figure 4(a) depicts the experimental (dots) and numerical (continuum line) values obtained for r against $z - z_{in}$ for $\alpha = 11$. The length Δz is indicated by the vertical lines wherein the r-values vary from 0.34 to 0.50. These r-values show that this method also minimizes the sidelobe effect along the ORB length even for a very narrow thickness below the Abbe's diffraction limit. Figure 4(b) depicts the transverse FWHM, Δx (experimental and numerical), as a function of $z - z_{in}$. The waist value $\Delta x_w = 24.3$ μm occurs at the ORB peak intensity at $z = z_w = 173.5$ μm measured from the Fourier plane located at $z = 0$, giving rise

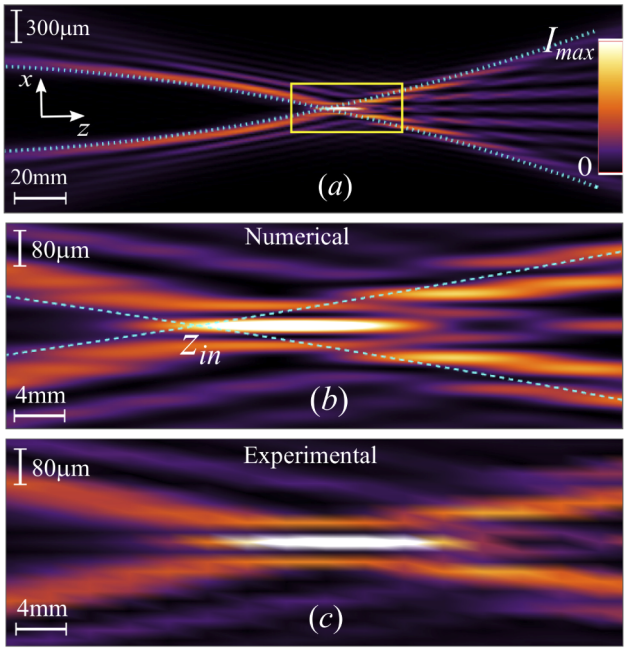

Fig. 3. (a) Intensity distribution of the ORB for $\alpha = 11$ in the xz-plane. Light-blue dashed curves are the caustic branches intersecting at z_{in}. A zoom of the framed box of (a) is shown on (b) numerical and (c) experimental. The different scales for x and z axes remark the ultra-long feature of the ORB.

OSA CONTINUUM

to the figure of merit $R = 640$. The gray curve is the on-z-axis intensity profile that follows an Airy-squared function. A slight variation in the ORB thickness, from 24 to 26μm, occurs along the whole Δz (inside the vertical lines), remarking the nondifracting feature of the beam. Finally, subfig. (c) shows the normalized cross-sectional intensity profile at beam waist, z_w. Numerical simulations are depicted in red continuum line while experimental values are the red dots. The sinc-squared pattern (black dotted line) of the top-hat beam is also depicted. It is confirmed $\Delta x_w = 24.3$ μm and $r = 0.34$, in accordance to subfigure (a). Hence, the width of the ORB is well below the Abbe's diffraction limit and it possesses a low sidelobe-to-central lobe intensity ratio. It is also shown in Fig. 4(c) that the sidelobe peak intensity of the ORB is greater than the corresponding to the sinc-squared profile. But it is important to highlight that the top-hat beam does not behave as a needle (it does the ORB) in the sense that the propagation distance in which the transverse size varies slightly is very short, in the order of two Rayleigh lengths.

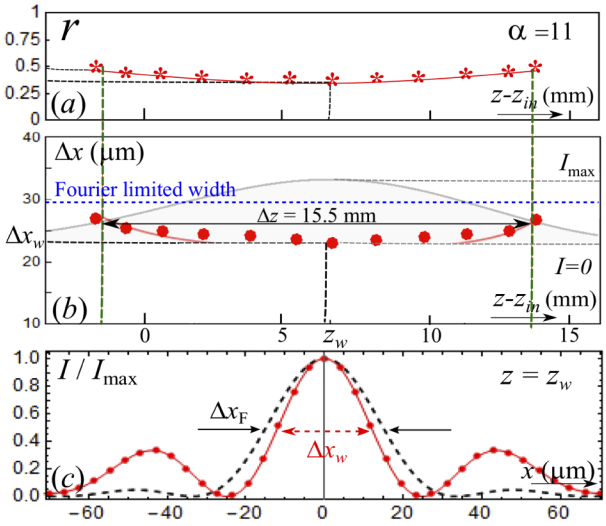

Fig. 4. (a) ORB sidelobe-to-main lobe intensity ratio and (b) thickness Δx against $z - z_{in}$. Vertical lines in (a)-(b) indicate the Δz extension. The gray curve in (b) is the on-axis intensity profile. (c) Transverse intensity profile along x for the ORB (red) and the sinc-squared pattern (black). Dots and stars are experimental values while lines are the numerical simulations.

ORBs have advantages to be implemented as an excitation source in LSM. Due to its caustic nature, the ORB has self-healing properties, in addition to the demonstrated nondiffracting ones, so that it can be used to reduce scattering and to provide a large FOV and an AR below the Abbe's diffraction limit. But, on the contrary to other exotic LS as Bessel and Airy ones, that are "virtually" generated scanning the laser digitally, ORBs are generated in the "real" modality allowing a simple and cost-effective deployment. By other hand, the ORB sidelobes are slightly more intense than the sidelobes of a Bessel beam with identical thickness (approximately one third more intense) but less intense (almost one half) than the first secondary lobe of the Airy beam. The advantage for the ORB is a relatively large separation between the main and sidelobe peaks (in the order of the sinc-squared pattern separation), which is a factor 1.3 and 2.1 larger than the separation for the Bessel and Airy beams, respectively. For this reason, the secondary lobes can be filtering more efficiently and should not have negative effects on the image quality for a proper microscope design.

OSA CONTINUUM

5. Conclusions

In summary, it was demonstrated, both numerically and experimentally, a newfangled approach to obtain ultra-long light sheets with width below the Abbe's diffraction limit. The approach is based on an induced intercrossing of the branches associated to a cusp curved beam via a spectral phase perturbation. The length and thickness of the resulting beam, the Optical Razor Blade (ORB), is fully tunable by the perturbation strength α. It was obtained an ORB with a width reduction close to 32% of the Abbe's diffraction limit with a low sidelobe-to-main lobe intensity ratio around 0.34 and a large length-to-width ratio greater than 640, remarking the efficiency of the method. The ORB has potential applications as the excitation source for light sheet microscopy (LSM). Even if the Bessel and Airy light sheets (LS) could possess better performance in some punctual feature with respect to the ORB, none of these LS meet simultaneously the global features of the ORB: to be a real LS (not generated from laser scanning), to be planar, to be below the Abbe's diffraction limit and to be ultra-long. Engineering of the ORB can be exploited in two ways: matching the FOV and the AR of the excitation and detection arms of the LSM to maximize the potential of the microscope and for the creation of custom-made excitation sources adapted to different sample requirements.

Funding

Ministerio de Ciencia e Innovación (PGC2018-095595-B-I00); Consejo Nacional de Investigaciones Científicas y Técnicas (CONICET-Argentina PIP-2015-2017 nro 11220150100435).

Disclosures

The Authors declare no conflicts of interest.

References

1. G. Chen, Z. Wen, and C. Qiu, "Superoscillation: from physics to optical applications," Light: Sci. Appl. **8**(1), 56 (2019).
2. R. Grunwald and M. Bock, "Needle beams: a review," Adv. Phys.: X **5**(1), 1736950 (2020).
3. Focus issue: super-resolution imaging, "Beyond the diffraction limit," Nat. Photonics **3**(7), 361 (2009).
4. E. T. F. Rogers, J. Lindberg, T. Roy, S. Savo, J. E. Chad, M. R. Dennis, and N. I. Zheludev, "A super-oscillatory lens optical microscope for subwavelength imaging," Nat. Mater. **11**(5), 432–435 (2012).
5. H. Nagar, T. Admon, D. Goldman, A. Eyal, and Y. Roichman, "Optical trapping below the diffraction limit with a tunable beam waist using super-oscillating beams," Opt. Lett. **44**(10), 2430–2433 (2019).
6. S. Jia, J. C. Vaughan, and X. Zhuang, "Isotropic three-dimensional super-resolution imaging with a self-bending point spread function," Nat. Photonics **8**(4), 302–306 (2014).
7. R. Schley, I. Kaminer, E. Greenfield, R. Bekenstein, Y. Lumer, and M. Segev, "Loss-proof self-accelerating beams and their use in non-paraxial manipulation of particles' trajectories," Nat. Commun. **5**(1), 5189 (2014).
8. B. K. Singh, H. Nagar, Y. Roichman, and A. Arie, "Particle manipulation beyond the diffraction limit using structured super-oscillating light beams," Light: Sci. Appl. **6**(9), e17050 (2017).
9. Z. Gan, Y. Cao, R. A. Evans, and M. Gu, "Three-dimensional deep sub-diffraction optical beam lithography with 9 nm feature size," Nat. Commun. **4**(1), 2061 (2013).
10. N. Shapira, Z. Deng, R. Remez, D. Singh, E. Katzav, and A. Arie, "Multi-lobe superoscillation and its application to structured illumination microscopy," Opt. Express **27**(24), 34530–34541 (2019).
11. S. Payeur, S. Fourmaux, B. Schmidt, J. MacLean, C. Tchervenkov, F. Légaré, M. Piché, and J. Kieffer, "Generation of a beam of fast electrons by tightly focusing a radially polarized ultrashort laser pulse," Appl. Phys. Lett. **101**(4), 041105 (2012).
12. H. Wang, L. Shi, B. Lukyanchuk, C. Sheppard, and C. T. Chong, "Creation of a needle of longitudinally polarized light in vacuum using binary optics," Nat. Photonics **2**(8), 501–505 (2008).
13. Y. Zha, J. Wei, H. Wang, and F. Gan, "Creation of an ultra-long depth of focus super-resolution longitudinally polarized beam with a ternary optical element," J. Opt. **15**(7), 075703 (2013).
14. L. Yang, X. Xie, S. Wang, and J. Zhou, "Minimized spot of annular radially polarized focusing beam," Opt. Lett. **38**(8), 1331–1333 (2013).
15. L. Turquet, X. Zang, J. Kakko, H. Lipsanen, G. Bautista, and M. Kauranen, "Demonstration of longitudinally polarized optical needles," Opt. Express **26**(21), 27572–27584 (2018).

OSA CONTINUUM

16. E. T. F. Rogers, S. Savo, J. Lindberg, T. Roy, M. R. Dennis, and N. I. Zheludev, "Super-oscillatory optical needle," Appl. Phys. Lett. **102**(3), 031108 (2013).
17. G. Yuan, E. T. F. Rogers, T. Roy, G. Adamo, Z. Shen, and N. I. Zheludev, "Planar super-oscillatory lens for sub-diffraction optical needles at violet wavelengths," Sci. Rep. **4**(1), 6333 (2015).
18. M. Li, W. Li, H. Li, Y. Zhu, and Y. Yu, "Controllable design of super-oscillatory lenses with multiple sub-diffraction-limit foci," Sci. Rep. **7**(1), 1335 (2017).
19. Y. Yu, W. Li, H. Li, M. Li, and W. Yuan, "An investigation of influencing factors on practical sub-diffraction limit focusing of planar super-oscillation lenses," Nanomaterials **8**(4), 185 (2018).
20. S. Banerji, M. Meem, A. Majumder, B. Sensale-Rodriguez, and R. Menon, "Extreme-depth-of-focus imaging with a flat lens," Optica **7**(3), 214–217 (2020).
21. E. Greenfield, R. Schley, I. Hurwitz, J. Nemirovsky, K. Makris, and M. Segev, "Experimental generation of arbitrarily shaped diffractionless superoscillatory optical beams," Opt. Express **21**(11), 13425–13435 (2013).
22. R. Martínez-Herrero, D. Maluenda, I. Juvells, and A. Carnicer, "Synthesis of light needles with tunable length and nearly constant irradiance," Sci. Rep. **8**(1), 2657 (2018).
23. P. Suresh, C. Mariyal, K. B. Rajesh, T. V. S. Pillai, and Z. Jaroszewicz, "Generation of a strong uniform transversely polarized nondiffracting beam using a high-numerical-aperture lens axicon with a binary phase mask," Appl. Opt. **52**(4), 849–853 (2013).
24. D. Panneton, G. St-Onge, M. Piché, and S. Thibault, "Needles of light produced with a spherical mirror," Opt. Lett. **40**(3), 419–422 (2015).
25. Z. Man, C. Min, L. Du, Y. Zhang, S. Zhu, and X. Yuan, "Sub-wavelength sized transversely polarized optical needle with exceptionally suppressed side-lobes," Opt. Express **24**(2), 874–882 (2016).
26. S. Zhang, H. Chen, Z. Wu, K. Zhang, Y. Li, G. Chen, Z. Zhang, Z. Wen, L. Dai, and A. Wang, "Synthesis of sub-diffraction quasi-non-diffracting beams by angular spectrum compression," Opt. Express **25**(22), 27104–27118 (2017).
27. M. Veysi, C. Guclu, O. Boyraz, and F. Capolino, "Reflective metasurface lens with an elongated needle-shaped focus," J. Opt. Soc. Am. B **34**(2), 374–382 (2017).
28. O. E. Olarte, J. Andilla, E. J. Gualda, and P. Loza-Alvarez, "Light-sheet microscopy: a tutorial," Adv. Opt. Photonics **10**(1), 111–179 (2018).
29. G. A. Siviloglou, J. Broky, A. Dogariu, and D. N. Christodoulides, "Observation of accelerating Airy beams," Phys. Rev. Lett. **99**(21), 213901 (2007).
30. M. V. Berry, *Catastrophe optics: morphologies of caustics and their diffraction patterns*, in Progress in Optics XVII, E. Wolf, ed. (North Holland, 1989).
31. P. Vaveliuk, A. Lencina, J. A. Rodrigo, and Ó. Martínez-Matos, "Caustics, catastrophes and symmetries in curved beams," Phys. Rev. A **92**(3), 033850 (2015).
32. P. Vaveliuk, A. Lencina, J. A. Rodrigo, and Ó. Martínez-Matos, "Symmetric Airy beams," Opt. Lett. **39**(8), 2370–2373 (2014).
33. D. Bongiovanni, Y. Hu, B. Wetzel, R. A. Robles, G. Mendoza González, E. A. Marti-Panameño, Z. Chen, and R. Morandotti, "Efficient optical energy harvesting in self-accelerating beams," Sci. Rep. **5**(1), 13197 (2015).
34. D. Amaya, Ó. Martínez-Matos, and P. Vaveliuk, "Abruptly autofocusing beams from phase perturbations having forced symmetry," Opt. Lett. **44**(15), 3733–3736 (2019).
35. J. W. Goodman, *Introduction to Fourier optics*, 3rd ed. (Roberts & Company, 2005) Chap.III-IV, pp. 55–85.
36. M. N. Zhu, Q. Cao, and Q. H. Gao, "Creation of a 50,000λ long needle-like field with 0.36λ width," J. Opt. Soc. Am. A **31**(3), 500–504 (2014).
37. P. Vaveliuk, A. Lencina, and Ó. Martínez-Matos, "Caustic beams from unusual powers of the spectral phase," Opt. Lett. **42**(19), 4008–4011 (2017).
38. E. Neyra, Ó. Martínez-Matos, and P. Vaveliuk, "Numerical simulations of the propagation properties of the Optical Razor Blade (ORB)," figshare (2020), https://doi.org/10.6084/m9.figshare.12597140.